The Performance and Scientific Rationale for an Infrared Imaging Fourier Transform Spectrograph on a Large Space Telescope

JAMES R. GRAHAM

Department of Astronomy, 601 Campbell Hall, University of California, Berkeley, CA 94720; jrg@astro.berkeley.edu

MARK ABRAMS

ITT Aerospace/Communications Division, 1919 West Cook Road, P.O. Box 3700, Fort Wayne, IN 46801; mcabrams@itt.com

C. BENNETT

Lawrence Livermore National Laboratory, MS L-043, P.O. Box 808, Livermore, CA 94550; bennett2@llnl.gov

J. CARR

Naval Research Laboratory, Code 7217, 4555 Overlook Avenue, Washington, DC 20375; carr@mriga.nrl.navy.mil

K. COOK

Lawrence Livermore National Laboratory, MS L-041, P.O. Box 808, Livermore, CA 94550; kcook@llnl.gov

A. DEY

Department of Physics and Astronomy, The Johns Hopkins University, 3400 N. Charles Street, Baltimore, MD 21218; dey@pha.jhu.edu

J. NAJITA

Space Telescope Science Institute, 3700 San Martin Drive, Baltimore, MD 21218; najita@stsci.edu

AND

E. WISHNOW

Lawrence Livermore National Laboratory and Space Sciences Laboratory, University of California Berkeley, MS L-401,
P.O. Box 808, Livermore, CA 94550; wishnow@llnl.gov

ABSTRACT. We describe a concept for an imaging spectrograph for a large orbiting observatory such as NASA's proposed Next Generation Space Telescope (NGST) based on an imaging Fourier transform spectrograph (IFTS). An IFTS has several important advantages that make it an ideal instrument to pursue the scientific objectives of NGST. We review the operation of an IFTS and make a quantitative evaluation of the signal-to-noise performance of such an instrument in the context of NGST. We consider the relationship between pixel size, spectral resolution, and diameter of the beam splitter for imaging and nonimaging Fourier transform spectrographs and give the condition required to maintain spectral modulation efficiency over the entire field of view. We give examples of scientific programs that could be performed with this facility.

1. INTRODUCTION

The Association of Universities for Research in Astronomy (AURA), with NASA support, recently appointed a committee to "study possible missions and programs for UV-Optical-IR astronomy in space for the first decades of the twenty-first century." The report urged the development of a general-purpose, near-infrared observatory equipped with a passively cooled primary mirror ($T \leq 70$ K) with a minimum diameter of 4 m (Dressler 1996). To enhance its performance, the report recommended that the observatory be placed as far from the Earth-Moon system as possible to reduce stray light and to maintain the telescope's relatively low temperature. With such a facility, it should be possible to learn in detail how galaxies formed, measure the large-scale curvature of spacetime by measuring distant standard candles, trace the chemical evolution of galaxies, and study nearby stars and star-forming regions for signs of planetary systems. A detailed discussion of the Next Generation Space Telescope (NGST) and its scientific potential is given by Stockman (1997).

For NGST to attain these scientific objectives, it must have an instrument that is designed to execute panchromatic observations over the critical 1–15 μm wavelength range of the faintest detectable objects. With nJy sensitivity levels attainable at near-infrared (NIR; 1–5 μm) and mid-infrared (MIR; 5–15 μm) wavelengths, NGST will be able to study the well-calibrated rest-frame optical diagnostics in distant ($z = 3$–10)

1205

galaxies, thus probing for the first time their stellar content, star formation history, and nuclear activity. At the longer wavelengths, NGST can investigate these properties in $z = 3$–5 galaxies using diagnostics that are unaffected by dust extinction and reddening and also study the dust properties directly.

At the flux limits characteristic of NGST, the confusion limit is likely to be approached, with virtually every pixel having significant information (e.g., by extrapolation from counts in the Hubble Deep Field; Williams et al. 1996). As a result, one of the best ways to maximize the scientific output from NGST is to provide a wide-field imaging spectrograph that is efficient in this limit.

An imaging Fourier transform spectrometer (IFTS) provides these capabilities in a low-cost, high-throughput, compact design. It provides the only efficient means of conducting *unbiased* spectroscopic surveys of the high-z universe, i.e., without object preselection (e.g., using broadband colors) and without the restrictions imposed by spectrometer slit geometry and placement. An IFTS also allows spectroscopy over a wide bandpass, affords flexibility in choice of resolution, is easy to calibrate, and is ideal for wide-field spectroscopic surveys. Bennett et al. (1993) and Bennett, Carter, & Fields (1995) describe the operating principles of imaging Fourier transform spectrographs and compare their performance with alternative imaging spectrometers. A comprehensive review of the application of interferometers and the techniques of Fourier spectroscopy to astrophysical problems is given by Ridgway & Brault (1984), and a recent summary of the field, including a description of an astronomical IFTS, is given by Maillard (1995).

Spaceborne Fourier transform spectrometers have been responsible for spectacular results in the fields of planetary exploration and cosmology. Infrared FT spectrometers developed at the Goddard Space Flight Center (GSFC) flew on board the *Mariner 9* mission to Mars and were carried to the outer planets by the *Voyager* spacecraft (Hanel et al. 1992). The instruments provided superb data revealing, for the first time, the composition of the atmospheres of the giant gaseous planets (e.g., Jupiter; Hanel et al. 1979). The Composite Infrared Spectrometer (CIRS), currently traveling to Saturn on board the *Cassini* spacecraft, is another instrument developed at GSFC. CIRS is the first step toward an imaging FTS as it has a linear array of detectors, rather than a single-element detector. CIRS will map the temperature and composition of the atmospheres of Saturn and Titan as a function of altitude during limb soundings (Kunde et al. 1996).

The definitive measurement of the spectrum of the cosmic microwave background radiation (CMBR) was one of the most dramatic experimental measurements of this decade (Mather et al. 1990; Gush, Halpern, & Wishnow 1990). The FIRAS instrument on board the NASA satellite *COBE* that first performed this measurement, and the COBRA rocket experiment conducted by the University of British Columbia that confirmed it a few months later, were both liquid-helium cooled, differential Fourier transform spectrometers. These instruments used a dual-input, dual-output configuration where one input viewed the sky and the other viewed a blackbody calibrator (Mather, Fixen, & Shafer 1993; Gush & Halpern 1992). Absolute photometric measurements were obtained by reference to the blackbody calibrator, and the CMBR was observed to have an undistorted Planck spectrum corresponding to a temperature of 2.728 ± 0.004 K (Fixen et al. 1996). The IFTS proposed here can be thought of as an extension of these experiments where focal plane detector arrays yield simultaneous imaging and spectral information.

In the next decade, missions such as WIRE, *AXAF*, and SIRTF will expand astrophysical horizons, possibly unveiling entirely new populations of objects. An IFTS offers the flexibility (e.g., spectral resolution) that may prove essential in investigating the nature of these sources. Because of its flexibility and its ability to provide simultaneous imaging and spectroscopy of every object in the field of view (FOV), an IFTS is a *necessary* instrument for the NGST mission.

2. IFTS CONCEPT

An IFTS (Fig. 1) is axisymmetric, and the optical path difference (OPD) is the same for all the points of the image with the same angle of incidence from the axis of the interferometer. Hence, the FOV is circular. On the object side, an entrance collimator illuminates the interferometer with parallel light. The interfering beams are collected by the output camera, creating a stigmatic relation between the object and image planes. By placing a detector array in the output focal plane, the entrance field is imaged on the array, and each pixel works as a single detector matched to a point on the sky.

Retrieving spectral information involves recording the interferogram generated by the source imaged onto the focal plane array (FPA). The OPD is scanned in discrete steps since FPAs are integrating detectors. Scanning in this way generates a data cube of two-dimensional interferograms. The signal from the same pixel in each frame forms an independent interferogram. These interferograms are Fourier transformed individually, yielding a spectral data cube composed of the same spatial elements as the image.

2.1. A Perfect Match to NGST Science

The features of an IFTS that make it the instrument of choice for NGST are efficiency, flexibility, and compactness. The most compelling reason for choosing an IFTS is that in the dual-port design (see Fig. 2), virtually every photon collected by the telescope is directed toward the focal plane for detection. Other solutions are inefficient, inflexible, and wasteful of mass, power, and volume. Cameras equipped with filters admit only a restricted bandpass at low spectral resolution. To compete with the spectral multiplex advantage of an IFTS, a camera system needs multiple dichroics and FPAs. The additional mass and thermal load is a severe penalty. Classical dispersive spectrographs have slit losses, grating inefficiencies due to light
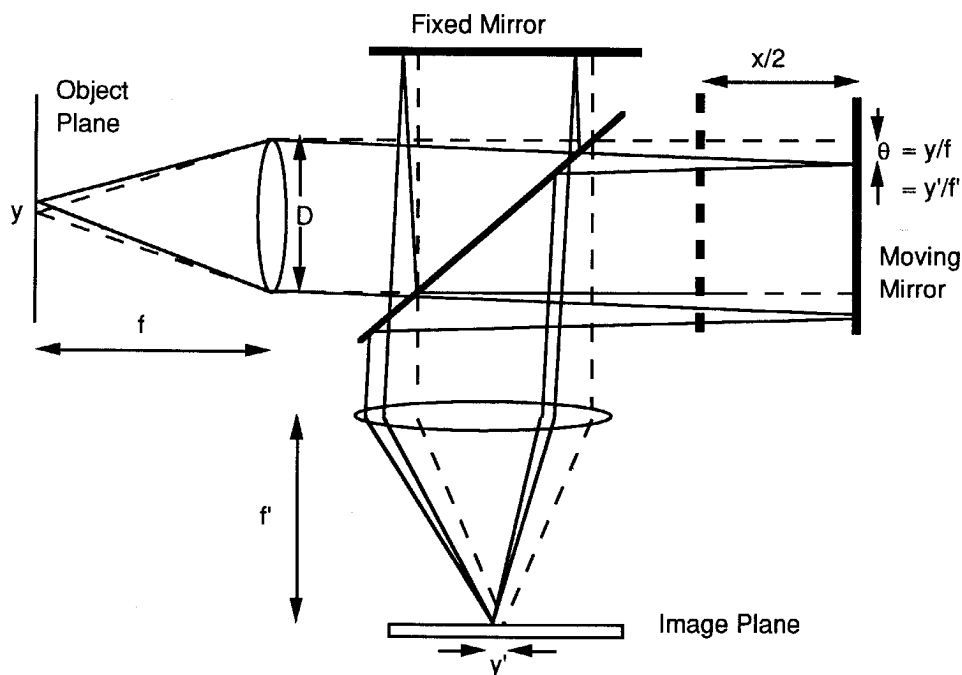
FIG. 1.—A sketch of the optics of a simple single-beam imaging Fourier transform spectrograph consisting of a collimating lens, a beam splitter, two mirrors (one movable), and a camera lens. The optical path difference is x.

lost in unwanted orders, and limited free spectral range (the same is true for a Fabry-Perot). *An IFTS acquires full bandpass imaging simultaneously with higher spectral resolution data.* Therefore, a high signal-to-noise ratio (SNR) broadband image always accompanies full spectral sampling of the FOV with

FIG. 2.—Schematic optical layout of a 60° dual-input, dual-output Michelson interferometer

no penalty in integration time. An IFTS is a true imaging spectrograph and measures a spectrum for every pixel in the FOV. It is not necessary to choose which regions in the image are most deserving of spectroscopic analysis. Overheads are eliminated because no additional observing time is needed for imaging prior to object selection, and there is no delay in positioning slit masks, fibers, or image slicing micromirrors. Thus, an IFTS will produce a rich scientific legacy with tremendous potential for serendipity.

Table 1 details the capabilities of an IFTS suitable for NGST. We use the instrument described by this table to illustrate the potential of an IFTS. Two points in Table 1 must be stressed: (1) An IFTS is spectrally multiplexed, therefore all spectral channels are obtained simultaneously within the stated integration time. (2) The free spectral range of an IFTS is limited only by the bandpass filter and the detector response. Consequently, the usual definition of resolution, $R = \lambda/\delta\lambda$, is of limited use. It is conventional to scan the OPD of an IFTS in equal steps so that the resolution is constant in wavenumber, k. Thus, we use M to denote the number of spectral channels. For example, in the NIR with a 1–5 μm bandpass, $M = 5$ means that $\delta k = (k_{max} - k_{min})/M = 1600$ cm^{-1}, and a scan yields five bands centered at 1.1, 1.3, 1.7, 2.3, and 3.6 μm.

The throughput of an IFTS with ideal optics is limited only by the efficiency of the beam splitter. In a dual-input, dual-output port design, no light is wasted and the throughput approaches 100%. An IFTS has no loss of light or spatial information because there is no slit, hence an IFTS is perfectly
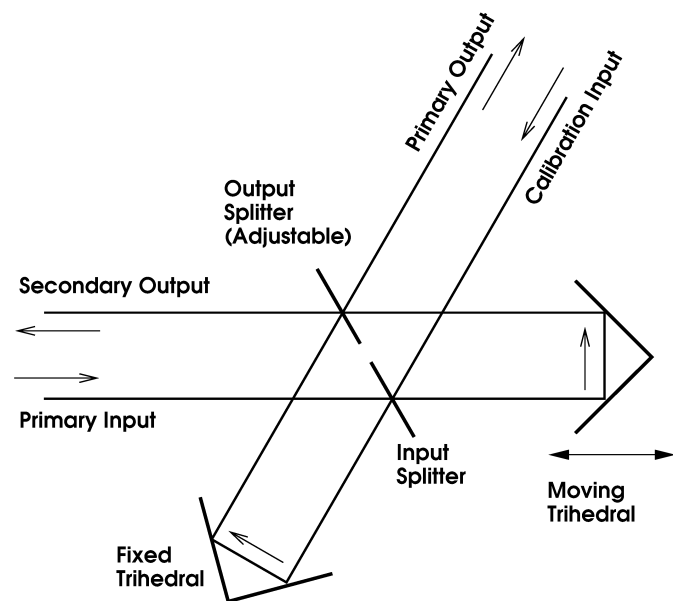
TABLE 1
CAPABILITIES OF A SPACEBORNE IFTS

Parameter	NIR Channel	MIR Channel
Design	Dual port	Dual port
Bandpass (μm)	1–5	5–15
Resolution (cm^{-1})	1	1
FOV (arcsec)	200	100
Pixel size (arcsec)	0.05	0.1
Array format	4K × 4K	1K × 1K
Detector	InSb	HgCdTe
Throughput	>0.5	>0.5
Sensitivity:[a]		
$M = 1$	200 pJy	13 nJy
$M = 5$	1 nJy	65 nJy
$M = 100$	35 nJy	1.3 μJy

[a] SNR = 10 for a 10^5 s integration over the entire spectral band for a point source. M is the number of simultaneous spectral channels in the bandpass (see § 2.1). Note that all spectral channels are obtained simultaneously. The spectrum is assumed to be flat in F_ν and the SNR is quoted at 2 μm for the NIR channel and at 10 μm for the MIR channel.

FIG. 3.—K-band number counts (Djorgovski et al. 1995; Gardner, Cowie, & Wainscoat 1993; Gardner et al. 1996; Glazebrook et al. 1994; Huang et al. 1997; Mobasher, Ellis, & Sharples 1986; Moustakas et al. 1997; McLeod et al. 1995; Metcalfe et al. 1996) together with models of the luminosity function modeled using the formalism of Gardner (1998), which has been used to extrapolate the number counts into the NGST domain. The solid lines include the effects of passive evolution, while the dashed lines include only K-corrections. The upper line in each case is for $q_0 = 0.1$, and the lower lines are for $q_0 = 0.5$. Current number counts imply at least 3500 objects per 3.′3 NGST field, while the extrapolations shown here suggest as many as 11,000 to $K = 29.5$.

adapted to doing multiobject spectroscopy in crowded or confusion-limited fields. A IFTS uses every photon, whereas traditional cameras and spectrographs throw away photons (either spectrally with a filter or spatially with a slit), so at a very fundamental level an IFTS is superior. On blaze, a good grating is 80% efficient, but averaged over the free spectral range this drops to about 65%. An IFTS is not optimized for single-object spectroscopy because the broadband photon shot noise is associated with every frame in the interferogram. Hence, for a single object a slit spectrograph is $\eta_g \eta_s M$ times faster than an IFTS of the same resolution in background-limited operation, where η_g is the grating efficiency averaged over the blaze function and η_s is the slit loss, where typically the product $\eta_g \eta_s \approx$ 0.3. This disadvantage is more than compensated for by the spatial-multiplexing capability of an IFTS. A typical deep background-limited exposure of an IFTS will reach $K = 29.5$, SNR = 10, and will contain at least 3500 and possibly, depending on cosmology, up to 11,000 objects per field (see Fig. 3). A grating spectrograph with a fiber feed or multislit capability can perhaps record spectra for only a few percent of these objects at a time, requiring hundreds of pointings to make an unbiased survey of a single field, as opposed to the single IFTS imaging-cum-spectroscopic observation.

An IFTS is tolerant of detector noise because it always operates under photon-limited conditions due to the broad spectral bandpass transmitted to the FPA. This is illustrated in Table 2, which shows a breakdown of the noise sources in the NIR and MIR channels corresponding to the performance listed in Table 1. Table 2 also shows that the readout rates required to avoid saturation are modest (1–10 mHz), since typical well depths for NIR InSb or HgCdTe arrays are a few 10^5 e^- and 10^7 e^- for MIR Si:As arrays.

Similarly, orders-of-magnitude higher thermal emission from the instrument, or thermal radiation leaks from outside the in-
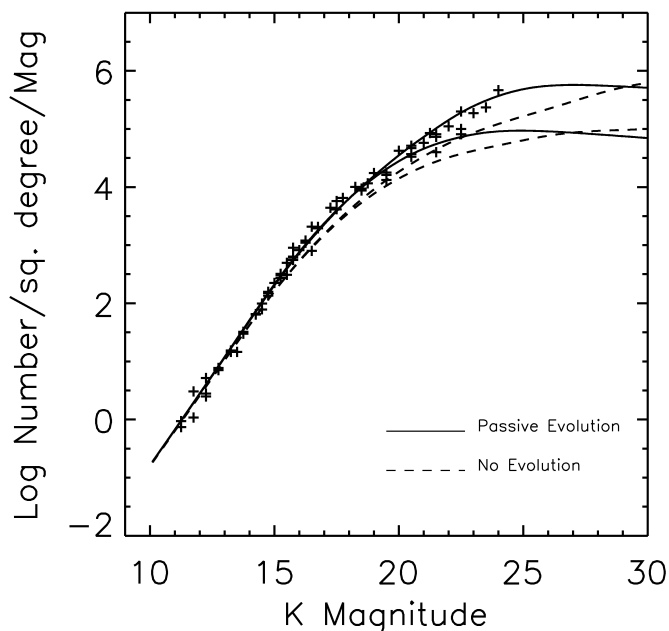
strument bay, can be tolerated compared with the case for dispersive spectrometers or fixed-filter cameras. As a pragmatic demonstration of this principle, the IFTS instruments LIFTIRS and HIRIS are routinely operated with ambient temperature optics in the 8–14 μm band (Bennett et al. 1995), whereas dispersive spectrometers, like SEBASS (C Bennett 1998, private communication), operating in the same spectral region, must have the slit and all following optics cooled far below ambient temperatures. The reason is that in a dispersive spectrometer the thermal emission of all the elements and optics downstream of the slit reach the detector at full spectral range determined by the bandpass-limiting element at or near the coldstop, whereas only the narrow spectral range corresponding to the width of a spectral channel for the signals of interest reach the detector pixels. For the IFTS, both the signals of interest and the thermal emission are seen over the full spectral range determined by the bandpass-limiting filter, and thus it is only necessary that the thermal emission of the optical elements along the optic axis integrated over the bandpass of interest be somewhat less than that of the integral of the zodiacal foreground, telescope emission, and source signal level integrated over the same broad spectral region.

An IFTS is potentially immune to cosmic-ray hits because

TABLE 2
Signal and Noise Budget

Parameter	NIR Channel	MIR Channel
F (nJy)	1	65
t (s)	1000	100
$\Delta\lambda(\mu m)$	1–5	5–15
Signal (electrons):		
Source	610	2709
Background[a]	3724	463669
Total signal	4334	466378
Noise (electrons rms):		
Signal shot noise	24.7	52.0
Background shot noise	60.8	680.9
Dark shot noise	5.5	10.0
Read noise	5	5
Total noise	66.0	683.0

[a] Background includes zodiacal foreground and thermal emission from the telescope as described in § 3.

the "energy" of a single upset pixel in one OPD frame appears as a sinusoidal signal divided among all bins in the spectral transform of the interferogram for that pixel. We can ignore cosmic-ray hits only if the counts generated are at or below our noise level. A minimum ionizing cosmic-ray proton ($E \simeq 1$ GeV) has ionization losses of $dE/dx \simeq 400$ eV μm^{-1} in Si. Assuming that 3.6 eV is required to produce an electron-hole pair, a cosmic ray will yield at least a few thousand events, because typical pixels have sensitive layers that are tens of microns thick. We would obtain a similar number for a hybrid device, i.e., InSb or HgCdTe on a Si multiplexer. If a cosmic-ray hit produces a significant signal in a certain number of pixels, those pixels must be "repaired" by interpolating the interferogram between the previous few "good" frames and the following few "good" frames that are not contaminated by cosmic-ray hits. The same sort of processing would be needed for any other system as well, be it an imager or a spectrometer. Comparison with the noise sources listed in Table 2 indicates that cosmic-ray hits will have to be repaired in the NIR channel, while the MIR channel will be more tolerant.

A dual-port design (Fig. 2) delivers the complementary symmetric and antisymmetric interferograms. In this dual-input, dual-output design, the field of the complementary input (labeled "Calibration Input" in Fig. 2) is also imaged and superimposed on each image of the "Primary Input." This property is often used to cancel the sky emission. In operation, when observing the sky in the primary input, the secondary input would be fed with a cold blackbody load, having negligible radiance. The final interferogram is constructed from the difference between the two outputs (which is therefore also immune to common-mode electrical noise), while the normalized ratio reveals systematic variation due to detector drifts.

The wavelength scale and the instrumental line shape (a sinc function if there is no apodizing) are precisely determined and are independent of wavelength. Absolute wavelength calibration is done by counting fringes of an optical single-mode laser. Compared with a dispersive system, the broadband operation

of an IFTS means that there are M times more photons for flat-fielding and determining signal-dependent gain (linearity). Hence, high signal-to-noise calibration images can be acquired faster or with lower power internal sources.

2.2. Pixel Size, Spectral Resolution, and Field of View

Spatial multiplexing renders the performance of an IFTS equal to that of an ideal multislit spectrograph (Bennett et al. 1995). Hence, even if we ignore slit losses and blaze inefficiency, the other advantages of an IFTS are overwhelming. The spectral resolution can be varied arbitrarily from the coarsest case of a small number of bands up to a spectral resolution limit determined only by the maximum OPD characteristic of the instrument. The proposed instrument has a maximum OPD of 1 cm and hence can operate over a range of resolutions from full band up to $M = 8000$ in the NIR.

The spectral resolution limit, $R = k/\delta k$, of a Michelson interferometer is

$$R = 8\left(\frac{d}{\phi D}\right)^2, \qquad (1)$$

where ϕ is the angular diameter of the FOV, d is the diameter of the beam splitter, and D is the telescope primary mirror diameter (e.g., Jacquinot 1954; Maillard 1995). Classically, ϕ refers to the entire field, but in the case of an IFTS, ϕ is the FOV of an on-axis pixel.

Although it is convenient if a single fringe fills the FPA, just as with an imaging Fabry-Perot, there is no reason why each pixel should record the same apparent wavenumber. Fringes crowd together with increasing field angle. Therefore, the need to maintain modulation efficiency over the entire field of view requires that the spatial separation of the fringes at the edge of the FPA, for a given retardance, is significantly greater than the pixel spacing.

If x is the OPD for a normally incident beam with wavenumber k, and θ is the field angle of off-axis rays at the beam splitter, then the path difference at θ is $x_\theta = x \cos \theta$ and the apparent wavenumber of this beam is

$$k_\theta = \frac{k}{\cos \theta}. \qquad (2)$$

The angles θ and ϕ are related by the angular magnification, D/d. If $\delta\theta$ is the angular width, also at the beam splitter, corresponding to a single pixel, the spectral resolution limit for off-axis points can be found by differentiating equation (2),

$$\frac{1}{R_\theta} = \frac{\delta k_\theta}{k_\theta} = \tan\theta\,\delta\theta, \qquad (3)$$

Figure 4 shows the pixel size for a given field of view for a range of resolutions. For example, for an 8 m diameter pri-
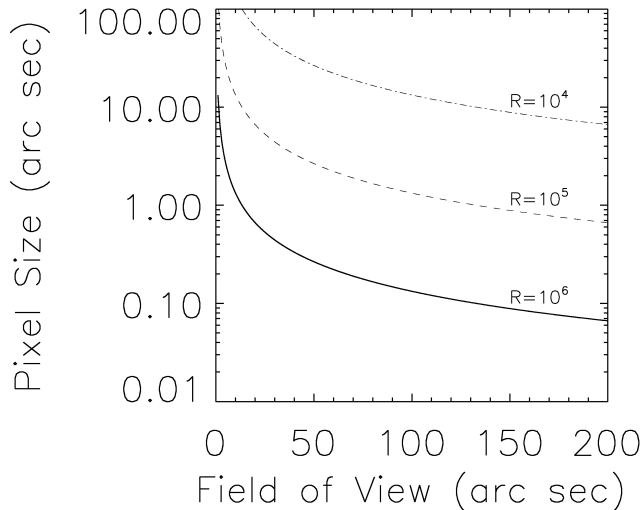
Fig. 4.—Pixel size as a function of the field of view required to spatially fully sample fringes at the edge of the FPA and hence maintain modulation efficiency. Curves are plotted for resolutions $R = k/\delta k = 10^4$, 10^5, and 10^6 assuming an 8 m diameter primary aperture and a beam splitter of diameter 10 cm.

mary aperture and a beam splitter of diameter 10 cm and an FOV of 200″, a pixel size of 0″.05, leads to a resolution limit of $R = 1.3 \times 10^6$. Since this resolution is 2 orders of magnitude greater than we are proposing, it is clear that spectral resolution is not the principal factor determining pixel size. An alternative way to view this constraint is that d, i.e., the size of the optics, is determined not by spectral resolution but by the requirement that there be no vignetting over the field of view. Thus, the optics for an IFTS are similar to those of a simple reimaging camera and are smaller and slower than those of an equivalent dispersive spectrograph.

We therefore have broad freedom to choose the pixel size by trading off field of view and spatial sampling. Given that NIR arrays of 4096 × 4096 pixels are likely to be available in the near future, a pixel size of 0″.05 yields a 3′.3 field of view and $\lambda/2D$ sampling at 4 μm. This choice of pixel size does not preclude diffraction-limited imaging at shorter wavelengths. If pixels have sharp boundaries, then it is possible to extract information at spatial frequencies above the cutoff in the pixel-sampling modulation transfer function if the spacecraft can offset and track at the subpixel level (cf. Fruchter & Hook 1998). Similar reasoning suggests 0″.1 pixels would be a satisfactory compromise for the MIR channel.

3. SIGNAL-TO-NOISE CALCULATIONS

An IFTS views all frequencies in its passband simultaneously but multiplexes them by modulating each optical frequency in the source at an "acoustic" frequency proportional to the optical frequency. Near the zero phase difference point of the interferometer, assuming an ideal beam splitter, full intensity is

transmitted through one port of a dual-port interferometer and no intensity through the other. For reasonably high resolution, most of the points in the interferogram are acquired away from the centerburst, and thus, to a good approximation, the average intensity transmitted through *each port* is 50% of the source intensity. In the time domain, the average signal photoelectron count rate for a dual-port interferometer is

$$\dot{N}_s = \int_{k_{\min}}^{k_{\max}} \eta(k)S_k dk, \qquad (4)$$

where S_k is the source photon rate per unit wavenumber and η is the system efficiency, including the telescope, collimator, beam splitter, and camera throughput and the detector QE. The integral is taken over the full bandpass of the system. The SNR in the time domain is given, on average, by

$$\mathrm{SNR}_t = \frac{\dot{N}_s t}{[t \int_{k_{\min}}^{k_{\max}} \eta(k)(S_k + B_k)dk + 2(tI_d + n_r^2)]^{1/2}}, \qquad (5)$$

where the noise consists of photon shot noise from source and background photon rate, B_k; dark current, I_d; and read noise, n_r. The integration time per OPD step is t. The factor of 2 in dark and read noise occurs because of the twin FPAs required for a dual-port instrument.

The relation of the SNR in the spectral domain to the SNR in the temporal domain can most easily be derived using Parseval's theorem. If there are N frames in the interferogram, the relation of the noise level in the spectral domain, σ_k, to the noise in the time domain, σ_t, assuming that it is approximately white, is given by

$$|\sigma_k|^2 = N^{-1}|\sigma_t|^2. \qquad (6)$$

Hence, the SNR in the frequency domain is

$$\mathrm{SNR}_k = N^{1/2} \frac{\mathrm{SNR}_t}{M}, \qquad (7)$$

where the last equality is obtained under the assumption of a white spectrum extending over M spectral channels. The SNR for an IFTS at any given resolution simply scales as $1/M$ per spectral channel.

For all SNR calculations (Table 1 and values in § 4) we have assumed a dual-port design on a 8 m telescope and $\eta = 0.5$. The background consists of zodiacal light at 1 AU and thermal emission from the telescope. The internal background within the IFTS is orders of magnitude lower than the external background because we expect that the IFTS optics and detectors will operate in the same low temperature ($\simeq 30$ K) environment within the NGST instrument bay. Therefore, the internal background has been neglected. We have used the zodiacal emission
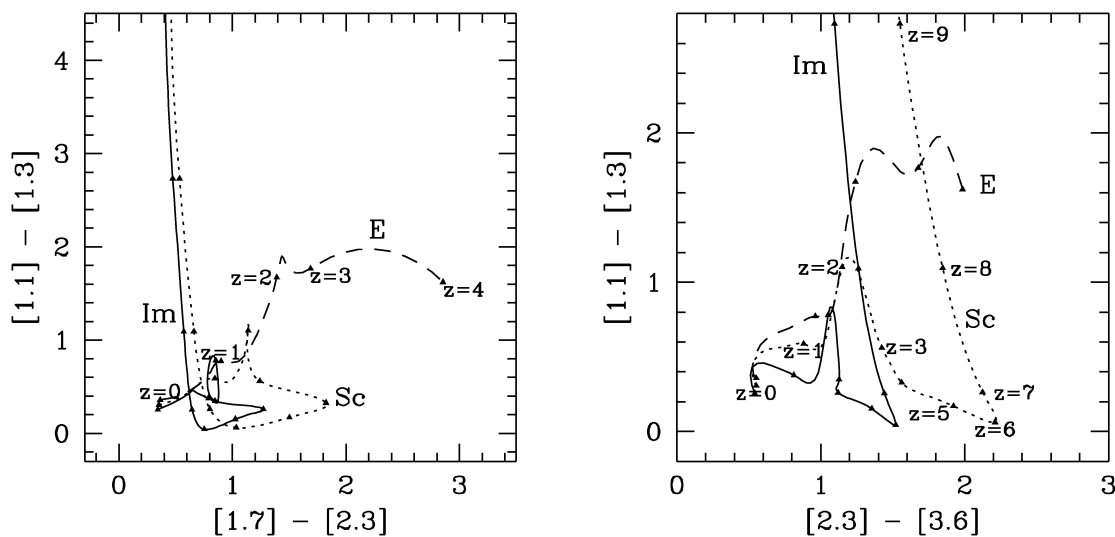
Fig. 5.—Colors for Im, Sc, and E galaxies as a function of redshift in five 1600 cm^{-1} wide passbands centered at 1.1, 1.3, 1.7, 2.3, and 3.6 μm. Colors are plotted from $z = 0$–10; a triangle is plotted at every interval of unit redshift. These curves assume unevolving models and only account for the K-corrections and the intergalactic absorption due to H I (this is only important at $z > 8$ at 1.1 μm). Thus the low-resolution IFTS colors provide a powerful measure of the age of stellar populations and photometric redshifts. In a typical 10^5 s exposure ($K = 29.5$, SNR = 10), the IFTS can do a good job of separating high-z objects from foreground objects.

measured at the ecliptic pole (Hauser et al. 1984) and include thermal background from the telescope optics, assuming $T = 50$ K and an emissivity of 0.06. The SNR results simulate optimal extraction of synthetic aperture photometry of a point source from a digital image. The size of the aperture that maximizes the SNR depends on the dominant noise source and on the wavelength and ranges between $\theta_{50} = 1.07\lambda/D$, i.e., the angular diameter that encircles 50% of the light, and $\theta_{80} = 1.79\lambda/D$.

The instrument performance depends on the detector dark current and read noise. For the NIR channel we assume a dark current of 0.03 e^- s^{-1} and an rms read noise of 5 e^- (with Fowler sampling; Fowler & Gatley 1990). For the MIR channel we assume a dark current of 1 e^- s^{-1} and an rms read noise of 5 e^-. This performance is optimistic, but not unrealistic, given projected detector development for NGST.[1]

4. NGST-IFTS SCIENCE

The versatility, broad wavelength coverage, and spatial multiplexing capability of an IFTS renders it well suited to executing a large space telescope's broad range of science goals. In this section, we discuss the applications of an IFTS that are representative of the many programs that can be carried out with this instrument.

4.1. Galaxy Formation

Since the rest-frame optical emission of distant galaxies is redshifted to the NIR, broadband, wide-field IR imaging surveys are essential to the study of their formation, early evolution, and merging history. The NIR colors synthesized from a low-resolution, five spectral channel IFTS survey offer excellent separation of galaxy type and redshift throughout the range $z = 1$ to $z < 10$ (Fig. 5). Thus, high-z galaxies can be picked out from foreground objects and a preliminary determination of their stellar populations made. An IFTS provides this capability along with the flexibility to conduct much higher spectral resolution surveys.

With an integration time of 10^5 s per 3$'$.3 FOV, an IFTS will obtain an SNR = 5–15 at the 1 nJy flux level in each of the five spectral channels; measure dwarf (rest-frame $M_B = -18.7$) star-forming irregular galaxies at $z = 5$ at an SNR = 40; and detect LMC-like star-forming systems or super–star clusters that might be representative of proto–globular clusters forming stars at 1 $M_\odot$ yr^{-1} for 25 Myr out to $z \approx 10$ and, if they exist, dwarf elliptical galaxies ($M_B = -15$) to $z = 3$ (Fig. 6).

Extrapolating the K-band galaxy luminosity function (see Fig. 3), taking only passive evolution into account, predicts that a 10^5 s $M = 5$ IFTS observation will yield high SNR (≥ 6) multicolor photometry for about 11,000 objects per field (for $q_0 = 0.1$; for $q_0 = 0.5$, there should be at least 3500 sources). Hence, in this mode, an IFTS can probe the evolution of the luminosity function as a function of morphological type and
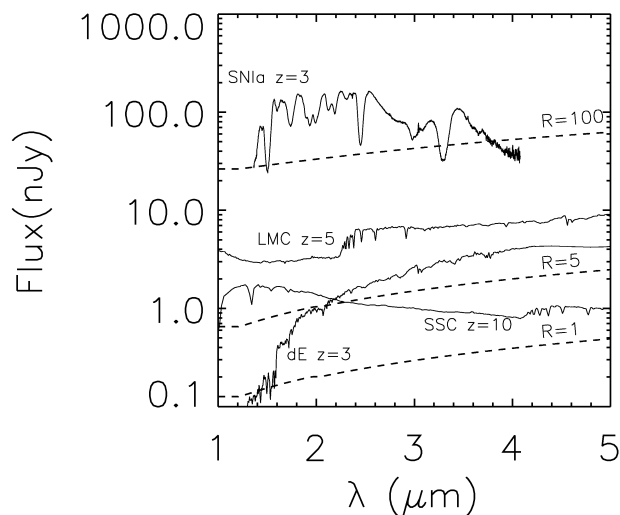
FIG. 6.—Sensitivity of IFTS in a 10^5 s exposure. See § 3 for details. The full 1–5 μm bandpass is scanned, and the flux corresponding to SNR = 10 is plotted as a dashed line. Spectral resolutions of $M = 5$ spectral channels (broadband imaging) and $M = 100$ spectral channels (low-resolution spectroscopy) are shown. Also shown are the spectra of a Type Ia supernova (SNIa), an LMC-like Magellanic irregular ($M_B = -18.7$), a dwarf elliptical ($M_B = -15$), and a super–star cluster (SSC), representative of a proto–globular cluster, forming stars for 25 Myr at 1 $M_\odot$ yr^{-1} $H_0 = 50$ km s^{-1} Mpc^{-1}, and $q_0 = 0.1$.

stellar content and thereby determine the spectral and merging history of galaxies. In addition, collapsing the interferogram yields an exquisitely deep (20 pJy rms!) 1–5 μm broadband image, enabling a morphological study of the faintest and very lowest surface brightness sources.

In a low-resolution spectroscopic mode (e.g., $M = 100$ spectral channels), an IFTS can yield spectroscopic redshifts (accurate to $\delta z \simeq 0.02$), explore the stellar population age and measure gas abundances in galaxies, and make extinction-free measurements of the star formation history of the universe. For a typical exposure of 10^5 s, an $M = 100$ IFTS observation reaches $K = 25.7$ (35 nJy) at SNR = 10 per spectral channel and should detect about 4500 sources to this limit in a single FOV ($q_0 = 0.1$). The spectral resolution is sufficient to detect standard H II region diagnostics (e.g., Paα at $z = 0$–2, Hα and [O III] at $z = 0.5$–10, Lyα at $z > 6$) and well-studied stellar features (e.g., 4000, 2900, and 2640 Å spectral breaks). At the detection limit (40 nJy), IFTS will be sensitive to star formation rates as low as 1–10 $M_\odot$ yr^{-1} for galaxies at $z = 3$–7 (Kennicutt 1983). Moreover, Hα is a more robust measure of the star formation rate than are rest-frame UV diagnostics, because it is relatively insensitive to dust extinction. For example, the intrinsic star formation rates in the $z = 2.5$–3.5 Lyman drop galaxies are likely to be greater than 100 $M_\odot$ yr^{-1}—factors of a few above the rates estimated from their rest-frame 1500 Å luminosity (Steidel et al. 1996). As such, the $M = 100$ IFTS survey will provide an accurate measure of the star formation history of the universe to $z \simeq 5$. For L^* ($M_B = -21$) star-form-

ing galaxies, the 2640, 2900, and 4000 Å spectral breaks can be measured to SNR = 40 out to $z = 6$, yielding a measure of the mean (luminosity-weighted) age of the stellar population with an accuracy of less than 0.5 Gyr. Population synthesis modeling of the observed spectra can yield even more accurate measures of the relative ages and stellar content of galaxy samples and potentially provide an estimate for the first epoch of galaxy formation and a lower limit to the age of the universe.

4.2. Evolution of IR Galaxies

While only one-third of the bolometric luminosity of local galaxies is radiated in the IR (Soifer & Neugebauer 1991), there is growing evidence that this fraction is actually increasing with redshift. The deepest counts available from *IRAS* at 60 μm (Hacking & Houck 1987), which correspond to an average redshift of about 0.2 (Ashby et al. 1996), already suggest some evolution of the IR emission in the universe. A deep survey with the *Infrared Space Observatory* (*ISO*) at 15 μm has discovered a few objects at $z = 0.5$–1 with star formation rates much higher than deduced from the optical (Rowan-Robinson et al. 1997). These conclusions are reinforced by unexpectedly high far-IR and submillimeter source counts measured by *ISO* and the James Clerk Maxwell Telescope/SCUBA (Puget et al. 1997; Smail, Ivison, & Blain 1997).

Deep optical surveys (Lilly et al. 1995; Williams et al. 1996) probe the rest-frame UV luminosities of high-redshift galaxies, which can be converted into star formation rates under plausible assumptions about young stellar populations. Analysis of these data suggests that the star formation rate of the universe peaked at $z \simeq 1$ and then declined (Lilly et al. 1996; Madau 1996). This has led to claims that the primary epoch of star formation in the universe has been seen. However, the conversion of UV luminosities into star formation rates must take into account a correction for the luminosity fraction absorbed by the dust that is generally associated with young stars. Since this correction is uncertain for high-redshift galaxies, the star formation rates currently deduced from optical surveys alone might be substantially underestimated (Calzetti 1997). For high-redshift galaxies, the only current direct observational constraint is set by the recent detection of the cosmic far-IR background built up from the accumulated IR light of faint galaxies along the line of sight. The far-IR and submillimeter background light detected by *COBE* implies a star formation rate that is a factor of 2 above that inferred from optical galaxies in the Hubble Deep Field (Puget et al. 1996; Schlegel, Finkbeiner, & Davis 1997).

Mid-IR low-resolution spectroscopy can be used to search for dusty, star-forming galaxies at high redshift. Figure 7 shows a sequence of redshifted spectra representing an ultraluminous (10^{12} $L_\odot$) *IRAS* galaxy such as Arp 220, which is a prototype for a deeply embedded starburst (Guiderdoni et al. 1997). (Arp 220 is not an active galactic nucleus, as recent *ISO* spectroscopy and VLBI observations show; Genzel et al. 1997; Smith, Lons-
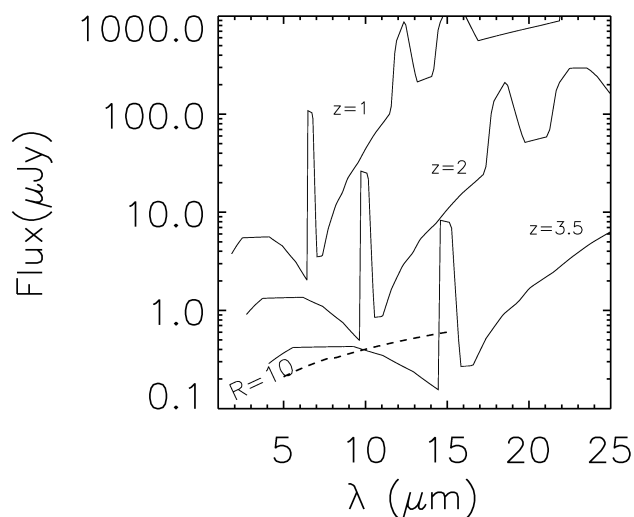
FIG. 7.—MIR spectra of an ultraluminous (10^{12} $L_\odot$) IR galaxy are plotted for $z = 1$–3.5 (Guiderdoni et al. 1997), representative of objects such as Arp 220. The most prominent narrow feature is the 3.3 μm PAH emission band. The sensitivity of IFTS in a 10^4 s exposure is shown. The full 5–15 μm bandpass is scanned, and the flux corresponding to SNR = 10 for $M = 10$ spectral channels is plotted as a dashed line. $H_0 = 50$ km s^{-1} Mpc^{-1}, and $q_0 = 0.1$.

dale, & Lonsdale 1998.) The most prominent feature in these spectra is 3.3 μm PAH emission that is shifted to the MIR band. Low-resolution MIR spectral scans will be exquisitely sensitive to this broad emission feature and therefore provide a sensitive way to search for deeply extincted star formation at high z. SIRTF will survey 1 square degree in the far-IR to a flux level of about 100 μJy to study the cosmological evolution of these sources. This detection threshold is sufficient to find about 200 ultraluminous IR galaxies to $z \simeq 3$. An NGST follow-up of the SIRTF square degree survey, lasting 1 month (330 fields × 10^4 s), would detect all these galaxies at high SNR in addition to many objects with lower star formation rates. The detection of redshifted PAH emission provides a unique signature of embedded star formation and protects against confusion with galactic cirrus, which limits the usefulness of longer wavelength searches.

4.3. Large-Scale Structure

The study of galaxy clustering is a classical test of theories of cosmic structure formation and a means of discriminating among cosmological world models. Since an IFTS acquires simultaneously both spatial and redshift information, it is the ideal instrument for the exploration of three-dimensional clustering. The 3′.3 FOV of our IFTS is well-matched to the size of clusters of galaxies at $z > 1$.

Foreground contamination will be a serious obstacle to the identification of high-z clusters, and obtaining spectra of very many (faint) galaxies is critical to establishing cluster membership and richness. Without redshifts, clusters might easily

go unnoticed. Since an IFTS obtains a spectrum for every pixel in the FPA, it is suited to the discovery and study of clusters. In particular, obtaining spectra of galaxies with complex morphologies (where slit placement would be difficult or wasteful of light) is straightforward with an IFTS. Examples include young galaxies that appear as a collection of small proto–globular cluster–sized clumps undergoing bursts of star formation (e.g., Tegmark et al. 1997) or galaxies undergoing merging.

IFTS spectral scans with 1000 spectral channels are well-suited to probing the velocity dispersion of rich clusters ($\gtrsim$1000 km s^{-1}). In a 10^5 s scan, an IFTS can obtain spectra throughout the 1–5 μm region of objects at the 800 nJy level (SNR = 5), i.e., L^* star-forming galaxies at $z \simeq 2$ or L^* elliptical galaxies, if they exist, at $z \simeq 3$. Emission-line diagnostics such as [O III] and Hβ are well-suited to probing the cluster velocity field. In addition, absorption lines such as NaI can be used to study the interstellar absorption of cluster galaxies (cf. Steidel et al. 1996).

Since we will simultaneously obtain high SNR rest-frame optical/UV morphology for these objects, it will be possible to study the virialization process and merging history of high-z clusters. These results, while interesting in and of themselves, will also complement future X-ray studies of the cluster virialization process to be carried out with *AXAF*.

Since a spectrum is obtained for every pixel, IFTS studies of clusters will also detect and obtain spectra for gravitational lens arcs and images. While the morphology and surface brightness structure of lensed images can be used to reconstruct the cluster mass distribution, their spectra can be used to probe the properties of very distant galaxies at high SNR (e.g., Franx et al. 1997).

4.4. Star and Planet Formation

Simultaneous broad wavelength studies of star-forming regions enable the study of stars, brown dwarfs, and planets at short wavelengths ($\lambda < 5$ μm) and their formation environments at longer wavelengths ($\lambda > 5$ μm). NGST can observe low-mass stars in star-forming regions out to several kiloparsecs and will map out the detailed properties of protoplanetary disks as a function of age, stellar mass, and environment in many star-forming regions with a total sample of thousands of stars. The unique ability of an IFTS to obtain colors and spectroscopy over a wide wavelength range for every object in the field makes it a powerful tool. Colors, reddening, luminosity, and spectral classification for every object will discriminate against cluster nonmembers, allow construction of Hertzsprung-Russell diagrams, and provide determination of cluster ages, age spreads, and measurement of the initial mass function.

The combination of the NIR and MIR channels of an IFTS can be used to determine the frequencies and lifetimes of protoplanetary disks and to understand the evolution of their dust and gas. While NIR excess emission traces hot dust near (0.1

AU) the star, the MIR is critical for probing material at planet formation distances. Spectra from 1–15 μm at $M = 50$ will provide detailed spectral energy distributions and yield radial disk structure, reveal gaps due to the presence of protoplanets, and determine dust composition from solid-state emission features. For stars in which active accretion has ceased, and in older clusters, an IFTS will provide sensitive MIR measurements of optically thin dust disks, the precursors of β Pic–like systems. Spectroscopy of the MIR rotational lines of H_2 will be used to determine the relative gas and dust dispersal timescales and place limits on the time for the formation of giant gas planets.

Star formation regions are ideal for the study of the substellar mass function and isolated superplanets because of the high stellar density and the brightness of substellar objects in their youth. An exciting prospect is the study of extrasolar giant planets (EGPs) that have been ejected from young planetary systems. The unexpected discovery that some Jupiter-mass planets orbiting nearby stars have highly eccentric orbits (Marcy & Butler 1996; Cochran et al. 1997) suggests that ejection of planets by dynamical scattering is a common outcome of the planet formation process (Lin & Ida 1997). These planets can be distinguished from free-floating EGPs that formed in isolation (via gravitational collapse) by their high proper motions, which will far exceed the velocity dispersions in young clusters. Very young (1 Myr) clusters are optimum for searching for ejected EGPs since they would be luminous and not have traveled far from where they formed. In addition, the high stellar density (10^2/FOV) provides a high probability of discovering ejected EGPs. Planets formed at AU distances will be ejected with velocities $\simeq 30$ km s^{-1}; in Orion this is a proper motion of 0''.06 in 5 yr, easily measured during the NGST lifetime. The discovery of high proper motion EGPs will provide a unique opportunity to study, via $M \simeq 100$ spectroscopy, the atmospheres of *true Jupiter analogs* (i.e., planets with a formation history similar to that of our own solar system) without the usual difficulties of studying orbiting planets in the glare of the central star.

An IFTS on NGST can be used to measure the mass function for substellar objects from brown dwarfs to superplanet masses on account of its ability to obtain photometry and spectroscopy of distant (>1 kpc), young open clusters. Such clusters are well matched to the FOV of our IFTS, and $M \simeq 100$ spectroscopy will provide spectral classification via H_2O and CH_4 bands of several hundred very low mass stars and substellar objects per cluster. At an age of 10 Myr, an IFTS can study free-floating superplanets of 5 M_{Jup} at a distance of 1 kpc in 10^5 s. Comparison of the atmospheric compositions implied by the spectral properties of ejected EGPs and those formed in isolation may confirm their different formation histories.

4.5. Kuiper Belt Objects

Kuiper Belt objects (KBOs) hold great significance for our understanding of the formation and evolution of the solar system, both as a source of short period comets and as primitive remnants of the planet-building phase of solar system history. One of the primary barriers to the detailed study of KBOs is that ground-based surveys do not reach deep enough limiting magnitudes to accumulate significant samples of objects. In addition, the high proper motion of KBOs (0''.5–2''.5 hr^{-1} for objects at 40 AU) requires that accurate orbital parameters must first be derived for precise slit placement in spectroscopic follow-up observations.

An IFTS offers the sensitivity and multiobject capability that is perfectly suited to discovery and follow-up spectroscopy of numerous, faint, high proper motion targets. In an IFTS survey of the ecliptic plane, KBOs would be detected by their characteristic proper motion observed in a series of images taken at each successive OPD. The corresponding interferograms for each detected object may be appropriately reregistered and stacked for Fourier transform recovery of the spectrum for each source. The spectrum of KBOs is a clue to their surface composition and collisional history.

Assuming a typical $R - K$ color for KBOs (e.g., Tegler & Romanishin 1997) and extrapolating the number counts at $R = 23$ (Jewitt, Luu, & Chen 1996) to the nJy level, an IFTS scan of 10^5 s over five spectral channels between 1–5 μm is sufficient to detect about 40 KBOs per 3''.3 FOV at SNR = 10. Much higher spectral resolution scans are feasible for brighter objects. From these data we would be able to construct a detailed census of objects between the orbit of Neptune and the Oort cloud and thereby provide a direct observation of the solar nebula and unique constraints on the dynamical history of the solar system.

5. CONCLUSIONS

An IFTS instrument can perform a wide variety of NGST science. The advantages of the IFTS concept are as follows:

1. Deep imaging acquired simultaneously with higher spectral resolution data over a broad wavelength range.
2. "Hands-off," unbiased, multiobject, slitless spectroscopy (ideal for moving objects). Efficient in confusion limit.
3. Flexible resolution ($M = 1$–10,000).
4. High throughput (near 100%) dual-port design.
5. Tolerant of cosmic rays, read noise, dark current, and light leaks.
6. Simple and reliable calibration. High SNR determination of flat fields and detector nonlinearity.
7. Compact, lightweight design. Slow reimaging optics.

REFERENCES

Ashby, M. L. N., Hacking, P. B., Houck, J. R., Soifer, B. T., & Weisstein, E. W. 1996, ApJ, 456, 428

Bennett, C. L., Carter, M., & Fields, D. J. 1995, Proc. SPIE, 2552, 274

Bennett, C. L., Carter, M., Fields, D. J., & Hernandez, J. 1993, Proc. SPIE, 1937, 191

Calzetti, D. 1997, in AIP Conf Proc. 408, The Ultraviolet Universe at Low and High Redshift: Probing the Progress of Galaxy Evolution, ed. W. H. Waller, M. N. Fanelli, J. E. Hollis, & A. C. Danks (New York: AIP), 403

Cochran, W. D., Hatzes, A. P., Butler, R. P., & Marcy, G. W. 1997, ApJ, 483, 457

Djorgovski, S., et al. 1995, ApJ, 438, L13

Dressler, A. 1996, Exploration and the Search for Origins: A Vision for Ultraviolet-Optical-Infrared Space Astronomy (Report of the *HST* and Beyond Committee) (Washington, DC: AURA)

Fixen, D. J., et al. 1996, ApJ, 473, 576

Fowler, A. M., & Gatley, I. 1990, ApJ, 353, L33

Franx, M., Illingworth, G. D., Kelson, D. D., van Dokkum, P. G., & Tran, K. 1997, ApJ, 486, L75

Fruchter, A., & Hook, R. 1998, Proc. SPIE, 3164, in press

Gardner, J. P. 1998, PASP, 110, 291

Gardner, J. P., Cowie, L. L., & Wainscoat, R. J. 1993, ApJ, 415, L9

Gardner, J. P., Sharples, R. M., Carrasco, B. E., & Frenk, C. S. 1996, MNRAS, 282, L1

Genzel, R., et al. 1997, preprint (astro-ph/9711255)

Glazebrook, K., Peacock, J. A., Collins, C. A., & Miller, L. 1994, MNRAS, 266, 65

Guiderdoni, B., Hivon, E., Bouchet, F. R., & Maffei, B. 1997, preprint (astro-ph/970340)

Gush, H. P., & Halpern, M. 1992, Rev. Sci. Instrum., 63, 3249

Gush, H. P., Halpern, M., & Wishnow, E. H. 1990, Phys Rev Lett, 65, 537

Hacking, P., & Houck, J. R. 1987, ApJSS, 63, 311

Hanel, R. A., et al. 1979, Science, 204, 972

Hanel, R. A., Conrath, B. J., Jennings, D. E., & Samuelson, R. E. 1992, Exploration of the Solar System by Infrared Remote Sensing (Cambridge: Cambridge Univ. Press)

Hauser, M. G., et al. 1984, ApJ 278, L15

Huang, J.-S., Cowie, L. L., Gardner, J. P., Hu, E. M., Songaila, A., & Wainscoat, R. J. 1997, ApJ, 476, 12

Jacquinot, P. 1954, J. Opt. Soc. Am., 44, 761

Kennicutt, R. 1983, ApJ, 272, 54

Kunde, V., et al. 1996, Proc. SPIE 2803, 162

Jewitt, D., Luu, J., & Chen, J. 1996, AJ, 112, 1225

Lilly, S. J., Hammer, F., Le Fevre, O., & Crampton, D. 1995, ApJ, 455, 75

Lilly, S. J., LeFevre, O., Hammer, F., & Crampton, D. 1996, ApJ, 460, L1

Lin, D. N. C., & Ida, S. 1997, ApJ, 477, 781

Madau, P., Ferguson, H. C., Dickinson, M. E., Giavalisco, M., Steidel, C. C., & Fruchter, A. 1996, MNRAS, 283, 1388

Maillard, J. P. 1995, in ASP Conf. Ser. 71, 3D Optical Spectroscopic Methods in Astronomy, ed. G. Comte, & M. Marcelin (San Francisco: ASP), 316

Marcy, G. W., & Butler, R. P. 1996, ApJ, 464, L147

Mather, J. C., et al. 1990, ApJ, 354, L37

Mather, J. C., Fixen, D. J., & Shafer, R. A. 1993, Proc. SPIE 2019, 168

McLeod, B. A., Bernstein, G. M., Rieke, M. J., Tollestrup, E. V., & Fazio, G. G. 1995, ApJS, 96, 117

Metcalfe, N., Shanks, T., Campos, A., Fong, R., & Gardner, J. P. 1996, Nature, 383, 236

Mobasher, B., Ellis, R. S., & Sharples, R. M. 1986, MNRAS, 223, 11

Moustakas, L. A., Davis, M., Graham, J. R., Silk, J., Peterson, B. A., & Yoshii, Y. 1997, ApJ, 475, 445

Puget, J. L., Abergel, A., Boulanger, F., Bernard, J. P., & Burton, W. B. 1996, A&A, 308, L5

Puget, J. L., et al. 1997, preprint

Ridgway, S. T., & Brault, J. W. 1984, AARA, 22, 291

Rowan-Robinson, M., et al. 1997, MNRAS, 289, 490

Schlegel, D. J. Finkbeiner, D. P., & Davis, D. 1997, preprint (astro-ph/9710327)

Smail, I., Ivison, R. J., & Blain, A. W. 1997, preprint (astro-ph/9708135)

Smith, H. E., Lonsdale, C. J., & Lonsdale, C. J. 1998, ApJ, 493, 17

Soifer, B. T., & Neugebauer, G. 1991, AJ, 101, 354

Steidel, C., Mauro, G., Pettini, M., Dickinson, M., & Adelberger, K. L. 1996, ApJ, 462, L17

Stockman, H. S. 1997, The Next Generation Space Telescope: Visiting a Time When Galaxies Were Young (Washington, DC: AURA)

Tegler, S. C., & Romanishin, W. 1997, Icarus, 126, 212

Tegmark, M., Silk, J., Rees, M. J., Blanchard, A., Abel, T., & Palla, F. 1997, ApJ, 474, 1

Williams, R. E., et al. 1996, AJ, 112, 1335